

# A Frequency-Modulated Continuous Wave Phased Array Marine Radar System Based on Smart Antenna Technology

Ruey-Bing (Raybeam) Hwang, Yi-Che Tsai, Chun-Fan Chien, Fang-Yao Kuo, Hsien-Tung Huang, Wei-Hsiung Chen, Cherng-Chyi Hsiao, Chin-Cheng Chuang, Ke-Wen Lin, Yuan-Hao Sun

**Abstract**—We describe an X-band marine phased-array frequency-modulated continuous-wave (FMCW) radar system based on the smart antenna technology. Two main features, including the beam-forming and angles-of-arrival (AOA) estimation, are presented in this paper. Such a system is composed of eight subarray antennas arranged linearly, each of which consists of ten 1-D patch array antennas generating a directional pattern along the vertical plane. The hybrid analog-digital beam-forming scheme was implemented; specifically, the phased local oscillator was developed for manipulating the phase angle over the local oscillator rather than over the output X-band signal for transmission. Alternatively, by dynamically adjusting the amplitude and phase of the FMCW signals generated by direct digital synthesis (DDS) device, we can also achieve the function of beam-forming. Additionally, the angles-of-arrival of the *correlated* echo signal scattering by targets are estimated by using the subspace method – space smooth multiple signal classification (MUSIC) algorithm. The AOA estimator, which includes the hardware for down-converting the X-band signals to I/Q baseband and the software for algorithm implementation, has been deployed. The measurements for range detection, angles of arrival estimation, and beam-forming has been carried out in this research work.

**Keywords**—FMCW, smart antenna system, phased-array system, angle-of-arrival estimation, beam-forming technique.

## I. INTRODUCTION

FMCW radar has been widely used in civilian and military applications of surveillance, tracking, precision ranging, medical diagnosis, and automotive collision avoidance [1], [2], [3], [4]. FMCW radars transmit broadband linear FM signal in a periodic swept time. Radar range resolution is inversely proportional to the FM bandwidth. The period of the swept time is longer than the round-trip time of the most distant target. FMCW radar receiver is typically a simple homodyne architecture that mixes the target echo with a replica of the transmit waveform. The beat frequencies can be determined through the fast Fourier Transform (FFT); the target ranges as well as speed can be obtained accordingly. As far as the mixing process is concerned, the linearity of the linear FM

signals is an important factor affecting the system performance. Specifically, the non-linearity of the FMCW waveform introduces extra spurious beating signals, enabling the occurrence of false alarms. The state-of-the-art direct digital synthesis (DDS) technique is now available to generate linear FM signals that simultaneously have acceptable linearity for required range resolution and spurious rejection.

Regarding the radar transmitter, the solid-state power amplifier (SSPA) is frequently used now as a power transmitter for some short range applications. Because the average transmitting power of SSPA, the FMCW radar can be comparable to that of a high peak-power and low duty-cycle pulse radar. Therefore, some short range pulse radars using cavity-resonant magnetron may gradually be replaced by SSPA FMCW radars. One type of FMCW radar uses a single antenna and a circulator to transmit and receive RF signals simultaneously. This type of FMCW radar always needs a self-cancellation circuit in front of the receiver low-noise amplifier (LNA) to suppress the self-interference. Another useful method to suppress the self-interference is to add metallic baffles outside the transmitting and receiving antennas for enhancing the isolation between them [5].

Beam-forming (or spatial filtering) technique entails an application of the phase weights to the element antennas of an array. The angular spectrum of the directivity pattern can exhibit constructive interference at particular (desired) angles but destructive interference at the other angles. For the radar system exploiting a mechanically scanned antenna, the high directivity beam pattern is scanned by using a gimbal-type servo. However, the phased-array radar system can steer its main beam with high directivity by using the beam-forming technique. The dynamic phased array has higher frame rates and is more robust in comparison to the antennas with mechanical beam steering. The beam-forming technique has been extensively investigated using schemes that use analog phase shifters and digital signal processing [6], [7]. From the view point of radar receivers, beam-forming can improve the signal-to-noise ratio by combining the signals coherently (weighted delay-and-sum), enabling the accuracy enhancement in target range- and direction- detection. On the other hand, beam-forming implemented in a transceiver is equivalent to spatial power combining, which coherently combines each of the signal radiating from the element antenna of an array. In our research work, the beam-forming is merely applied in the radar transmitter for improving the gain of the transmitter.

---

R. -B. Hwang, Y. -C. Tsai, C. -F. Chien, F. -Y. Kuo, H. -T. Huang, K. -W. Lin, C. -C. Hsiao, C. -C. Chung, and Y. -H. Sun are with the ECE Department, National Chiao Tung University, Hsinchu, 30010, Taiwan. W.-H. Chen is with the ZyFlex Technology, Hsinchu 30075, Taiwan. Corresponding author: Prof. Ruey-Bing Hwang with his email: raybeam@mail.nctu.edu.tw. This research is supported in part by the Ministry of Science and Technology, Taiwan under the contract: NSC 101-2221-E-009-097-MY2

It should be pointed out that the calibration process is critical to synthesizing a desired array pattern achieved by realizing the desired amplitude and phase distributions over the entire array. Some calibration techniques employ the antenna pattern, and modeling methods which include mutual coupling effects [8], [9] for this purpose. In this paper, calibration is implemented by tapping each transmitter output and down-converting into I/Q baseband to calculate the correction factors to the weights.

Array radars usually incorporate angle-of-arrival (AOA) estimation algorithms to search multiple targets. Eigen-structure method is widely used for AOA estimation in noisy environments [10]. A variety of AOA estimation algorithms are available for phased array systems; for example, Bartlett, Capon, Min-norm, MUSIC and ESPRIT [11], [12], [13], [14], [15]. Among these algorithms, MUSIC provides high resolution as well as accuracy, and is widely implemented in phased array radar systems. The Eigen-structure AOA algorithm forms a correlation matrix from a number of samples (snapshots) of the array elements, and then decomposes the correlation matrix into signal eigen-space and noise eigen-space. Based on the orthogonal property of these two sub-spaces, the angles of the incoming plane waves can be estimated through a search of the peaks of the pseudo-spectrum. The number of sources in the system is usually limited to the number of array elements. Unfortunately, the traditional MUSIC algorithm cannot handle correlated signals that typically arise in a radar scenario, and reduce the rank of the correlation matrix. Smoothed MUSIC algorithm was reported to be able to remove the correlation by calculating the smoothed correlation matrix, obtained by using the arithmetic mean of the correlation matrices corresponding to the overlapped subarrays subdivided from the original array [16], [17], [18].

This paper is organized as follows. Section II presents the principle of the FMCW radar, while Section III describes the phased-array FMCW radar architecture. Next, the hybrid analog-digital beamformer is introduced in Section IV. Section V discusses the angle-of-arrival estimation algorithm and its hardware implementation. Section VI presents the details of radar performance evaluation, angle and range detection, and those of the range resolution measurements. Finally, some concluding remarks are presented in Section VII to summarize the paper.

## II. PRINCIPLE OF AN FMCW RADAR

Figure 1 shows the function block diagram of an FMCW radar system, including the transmitter, the receiver and two isolated high-gain antennas. To obtain a highly linear FMCW sweep signal, we use a DDS to generate a linear up-down chirp FMCW signal with a swept frequency bandwidth  $B$ , which is centered at  $f_c$ , and has a sweep time  $T_s$ . The time-varying FMCW signal is generally written as:

$$S(t) = A \cos \left( 2\pi f_c t \pm \pi \frac{B}{T_s} t^2 \right) \quad (1)$$

where  $f_c$  is the carrier frequency and  $A$  is the amplitude of the FMCW signal. Note that in our system,  $B$  and  $T_s$  are 50 MHz (from 175 MHz to 225 MHz) and 0.25 ms, respectively.

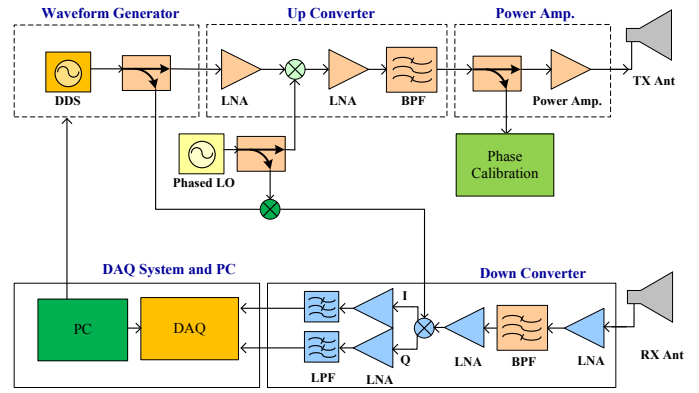


Fig. 1. Function block diagram of a typical FMCW radar system.

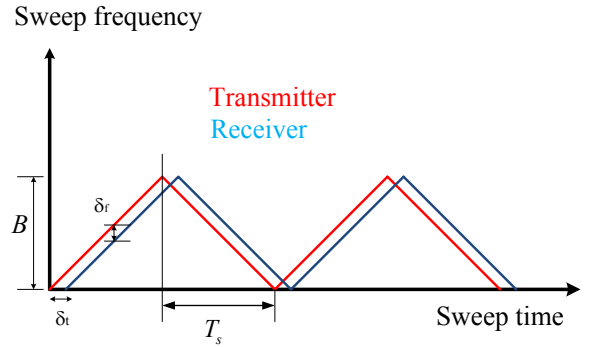


Fig. 2. The relation between the sweep frequency and sweep time for the transmitted and received FMCW signals.

Note that the plus sign in (1) represents the up-chirp signal, whereas the minus sign is associated with the down-chirp one.

As shown in Fig. 1, the baseband signal is up-converted to X-band centered at 9410 MHz by a 9210 MHz STALO (stable local oscillator). Following the up-conversion mixer is a bandpass filter to remove the lower sideband and unwanted signals such as the leakage from the LO. The X-band FMCW signal goes through a bandpass filter and a power amplifier, and is then delivered to a transmitting antenna for radiating. The echo signal from the target is received by the receiving antenna and is processed through a bandpass filter and a low-noise amplifier. Additionally, a homodyne receiver architecture is used; an IQ demodulator is used to convert the X-band echo signal directly to I and Q baseband through a local oscillator signal, which is a replica coupled from the transmitter (after the power amplifier) via a directional coupler. After sampling the I and Q data by using a data acquisition (DAQ) system, which is controlled by a personal computer system, we obtain the target information, including the range and speed of a moving target.

As shown in Fig. 2, the received waveform (blue) is simply a delay replica of the transmitted one. The frequency shift between the transmitted and received waveforms, denoted as  $\delta_f$  (beat frequency), can be directly read from the figure as far as the time delay is specified, which is prescribed as  $\delta_t$ . Thus,

the relation between the delay time and beat frequency can be readily obtained as:

$$\delta_t = \frac{\delta_f T_s}{B} \quad (2)$$

Note that  $\delta T$  is the round-trip time for the electromagnetic wave launched from the transmitter, reflected by the target, and returned to the receiver. The distance between the radar and target is then determined by:

$$R = \frac{C \delta_f T_s}{2B} \quad (3)$$

, where  $C$  is the speed of light in vacuum.

Furthermore, as mentioned previously the beat frequency between the transmitted and received signals can be directly obtained through a direct-conversion (zero-IF) receiver. Therefore, a multitude of pseudo-beat-frequencies will be exhibited if nonlinearities are present. Additionally, the range resolution ( $\Delta R$ ) of the FMCW radar system can be determined by using the equation below:

$$\Delta R = \frac{C}{2B} \quad (4)$$

Thus, an increase in the sweep bandwidth ( $B$ ) would enhance the range resolution for an FMCW radar system.

### III. PHASED-ARRAY FMCW RADAR ARCHITECTURE

In this work, we extend a commonly used single channel FMCW radar to a phased-array system containing 8 channels, each of which consists of a transmitter, a receiver, and subarray antennas. The 8 subarray antennas are arranged in a one-dimensional periodic nature with a period of 15.6 mm along the horizontal direction. The architecture, which is comprised of a transmitter and an array of 8 receivers was developed for the AOA detection. For this operating mode, only the angles of echo signals are detected. Once the angles of arrival has been determined, the beamformer, consisting of array of 8 transmitters and a receiver, is exploited to detect the range while scanning in the vicinity of the angles of arrival. For the single channel transmitter or receiver, their system architectures are the same as those of the traditionally ones. The main difference stems from the dynamic control and calibration of the amplitude as well as the phase angle on each channel. In this section, we will introduce the system architecture of an FMCW radar transceiver, including the active and passive components and antennas.

A typical FMCW radar system, shown in Fig. 1, contains a transmitter, a receiver, and two antennas for transmitting and receiving signals. The design of an FMCW radar begins with the link-budget calculation, which is dominated by the signal-to-noise ratio (SNR) of a receiver. The signal-to-noise ratio of a radar receiver can be evaluated by using the formula given below:

$$SNR = \frac{P_t G_t G_r \lambda^2 \sigma}{(4\pi)^3 k_B T B F_n L_s R^4} \quad (5)$$

, where  $P_t$  is the transmitted power;  $G_t(G_r)$  is the transmitting (receiving) antenna gain;  $\lambda$  is the operating wavelength;  $\sigma$  is the target radar cross section;  $k_B$  is the Boltzmann's constant equal to  $1.38e^{-23} \text{ Joule}/^\circ K$ ;  $T$  is the temperature in  $^\circ K$ ;  $B$  is the Fast Fourier Transform (FFT) resolution bandwidth;  $F_n$  is the noise figure of the receiver;  $L_s$  is the system loss; and  $R$  is the range between the target and radar. It is well known that not only the performance of range detection but also that of the angle-of-arrival detection is strongly related to SNR of each receiver. Consequently, SNR is the most critical issue in an FMCW radar receiver design.

Additionally, the phase noise of the stable local oscillator is an important factor affecting the SNR of a radar system. Let the minimum detectable signal-to-noise ratio at a radar receiver – be denoted as  $SNR$ . The parameter  $\Delta S$  is the power difference (in dB) between the unwanted and wanted signals, where the separation in frequency is denoted by  $\delta f$ . The unwanted signal defined here may be the result of direct coupling from the transmitter or due to reflection from nearby scatterers. The following equation can be used to determine the phase noise specification of a local oscillator.

$$S_{\Delta\phi} = -(SNR + \Delta S + 10 \log_{10} BW) \quad (6)$$

, where  $BW$  represents the FFT resolution bandwidth in Hz; the unit of the phase noise is  $\text{dBc}/\text{Hz}$ . For example, if we assume that  $\Delta S = 60 \text{ dB}$ ,  $SNR = 12 \text{ dB}$ , the FFT resolution bandwidth is 1 KHz, and  $\Delta f = 1 \text{ MHz}$ , then the phase noise will be  $-(12 + 60 + 10 \log_{10} 1000) = -102 \text{ dBc}/\text{Hz}$  at 1 MHz away from the center of the unwanted signal.

In a commonly used phased array system, a phase shifter is used to manipulate the phase angle of each RF signal delivered to the element antenna. Therefore, for a signal which has a wide bandwidth, the frequency response of a phase shifter must be taken into account and a sophisticated feedback control for phase calibration is absolutely essential. To overcome this drawback, we manipulate the phase angle over the single frequency generated by the STALO (stable local oscillator) rather than directly on the broadband RF signal. In the following section, the design of the phased local oscillator will be described.

#### A. Phased STALO (stable local oscillator)

The phased STALO is a phase adjustable stable local oscillator. A voltage-controlled oscillator (Mini-Circuits MOS-2360-119+) operating at 2302.5 MHz is connected to a voltage-controlled phase shifter (Mini-Circuits JSPHS-2484+). It is followed by a multiplier made of an Infineon Silicon Germanium RF transistor, operating in the non-linear region, to obtain the harmonics of the input signal. A subsequent high-Q bandpass filter, which will be described later on, selects the desired harmonic frequency, which is, 9210 MHz, and filters out the other harmonics and fundamental from the output. The phase noise of the VCO at 2302.5 MHz is  $-122 \text{ dBc}/\text{Hz}$  at 1 MHz offset. Through the  $\times 4$  multiplier, its phase noise degrades to  $-110 \text{ dBc}/\text{Hz}$  at 1 MHz offset. However, it is still acceptable according to the rule of thumb mentioned in the previous section.

## B. Passive components

The microwave band-pass filter (BPF) is an essential component for removing the unwanted signals and allowing the desired signals to pass. As far as a band-pass filter is concerned, we need to take three factors into account, namely the return loss, the insertion loss, and the variation of the group delay in the passband. Additionally, to provide a sufficient image rejection for the signal through a nonlinear device, frequency selectivity is also an important factor to be considered for bandpass filter design. To enhance the frequency selectivity, many BPF stages are cascaded; however, the insertion loss is then increased dramatically. Therefore, the design tradeoff is always an issue, particularly for the receiver design (system loss in the SNR equation in (5)).

1) *Six-pole BPF*: The six-pole Chebyshev bandpass filter with a 0.01-dB ripple level was designed to suppress the lower side-band signal from 8985 MHz to 9035 MHz, generated by an up-conversion mixer in the transmitter, as well as by the LO leakage. Since the LO (at 9210 MHz) and the upper side-band (from 9385 MHz to 9435 MHz) signals are very close to each other, a BPF with high frequency selectivity is required. Here a six-pole BPF with the center frequency and bandwidth of 9500 MHz and 320 MHz was synthesized based on the design rule [19], [20], with the coupling coefficients and the external quality factor given below:

$$\begin{aligned} M_{12} &= M_{56} = 0.033 \\ M_{23} &= M_{45} = 0.022 \\ M_{34} &= 0.021 \\ Q_{ext} &= 23.19 \end{aligned} \quad (7)$$

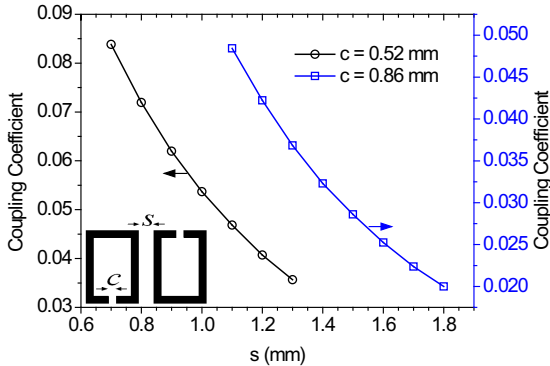


Fig. 3. Simulated coupling coefficients *versus* the distances between the resonators.

Here, an open-loop resonator is taken as the basic unit cell for the BPF design. The open-loop resonator has a half-wavelength perimeter at a center frequency of 9500 MHz as shown in Fig. 3. The resonator was printed on a microwave substrate with a relative dielectric constant of 3.38, loss tangent of 0.0027, and a thickness of 32 mil. The coupling coefficient for various separation distances between the two resonators can be extracted from numerical simulations by using the CST Microwave Studio [25]. Using Fig. 3, and the coupling

coefficients given in (7), we may determine the separation distances between the two adjacent resonators that are given by:  $d_{34} = 1.65$  mm,  $d_{23} = d_{45} = 1.59$  mm,  $d_{12} = d_{56} = 1.28$  mm,  $d_f = 0.51$  mm, the other relevant parameters are  $c = 0.86$  mm and  $L_f = 4.43$  mm. The physical circuit layout is shown in Fig. 4.

Fig. 5 shows the measured results with the photograph of the six-pole bandpass filter attached. The size of the filter is 22.9 mm by 5.9 mm, i.e.,  $0.73 \lambda_g$  by  $0.19 \lambda_g$ , where  $\lambda_g$  is the guided-wave wavelength at the center frequency. Note that a 35 dB suppression for the lower sideband signal has been achieved. Moreover, the reduction of LO leakage at 9210 MHz is up to 25 dB.

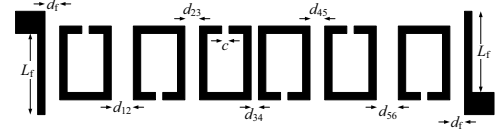


Fig. 4. Circuit layout of the Six-pole band-pass filter at a center frequency and bandwidth of 9500 MHz and 320 MHz.

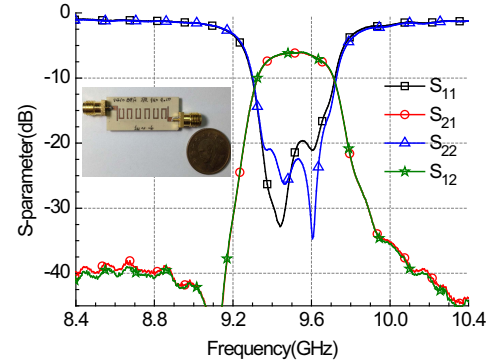


Fig. 5. Measured results of the six-pole bandpass filter.

2) *Four-pole BPF*: The next BPF to be presented is used for the purpose of selecting the fourth harmonic of the input signal via the  $\times 4$  multiplier. The four-pole Chebyshev bandpass filter with a 0.01 dB ripple level was employed (see Fig. 6). The center frequency of the bandpass filter is set to 9210 MHz, with the bandwidth of 500 MHz. The coupling coefficients and the external quality factor corresponding to the design specification are given below:

$$\begin{aligned} M_{12} &= M_{34} = 0.058 \\ M_{23} &= 0.043 \\ Q_{ext} &= 13.12 \end{aligned} \quad (8)$$

Repeating the design procedure that we have presented previously, the distance between the adjacent resonators can be determined. They are:  $d_{23} = 1.1$  mm,  $d_{12} = d_{34} = 0.94$  mm,  $d_f = 0.4$  mm,  $c = 0.52$  mm, and  $L_f = 4.5$  mm. The measured S-parameters and the photograph of the four-pole band-pass filter was shown in Fig. 7. The length of the filter

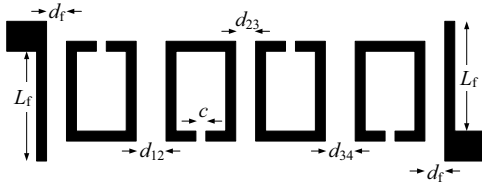


Fig. 6. Four-pole bandpass filter at a center frequency 9.21 GHz.

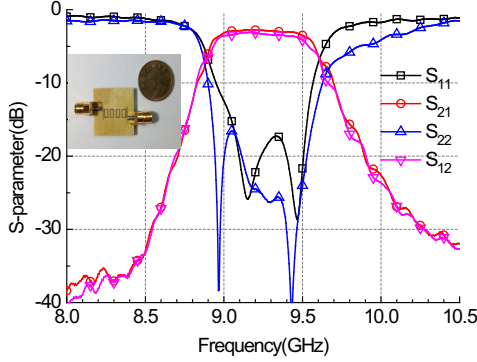


Fig. 7. Measured S-parameters and the photograph of the four-pole bandpass filter.

is 13.7 mm and its width is 6.4 mm, i.e., its dimensions in wavelength are  $0.42 \lambda_g$  by  $0.20 \lambda_g$ , where  $\lambda_g$  is the guided wavelength on the substrate at 9210 MHz.

3) *Bandpass Filter with SIRs at a Center Frequency of 2302.5 MHz:* To filter out the spurious harmonics generated by the VCO, a BPF based on the stepped-impedance resonators (SIRs) [21], [22], [23] was designed to achieve wide band rejection for the unwanted harmonics. The center frequency of the BPF was designed to be 2302.5 MHz, with a bandwidth 50 MHz. The impedance ratio ( $Z_2/Z_1$ )  $R = 0.3$  and the length ratio ( $\theta_2/(\theta_1 + \theta_2)$ )  $u = 0.7$  were chosen to extend the rejection band to  $3f_0$ . Figure 9 shows the measured results with the structure attached. The structure parameters of the BPF are:  $s = 1.3$  mm,  $L_1 = 2.8$  mm,  $L_2 = 6.9$  mm,  $W_1 = 0.3$  mm and  $W_2 = 6$  mm. The size of the filter is 19.4 mm by 13.3 mm, i.e.,  $0.15 \lambda_g$  by  $0.10 \lambda_g$ , where  $\lambda_g$  is the guided wavelength at 2302.5 MHz. From the measured result shown in Fig. 9, the rejection bands was extended up to 7 GHz for a 17 dB attenuation.

### C. Active components

The active components comprise of a low-noise amplifier, a power amplifier, and a voltage-controlled oscillator. The output P1dB is 34 dBm at 9410 MHz, with a gain of 31.5 dB for the power amplifier (Hittite HMC-952). The output P1dB is 18 dBm at 9410 MHz, with the noise figure of 4.4 dB for the low-noise amplifier (Mini Circuit AVA-183A+). The output power of the VCO (Mini Circuit ZX95-2490+) is 13.1 dBm at 2302.5 MHz.

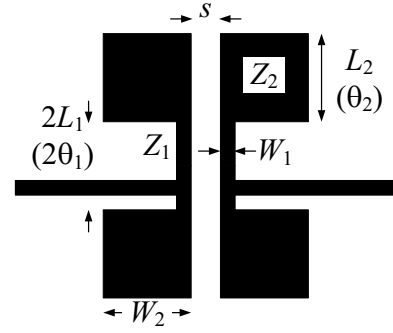


Fig. 8. Bandpass filter with SIRs at a center frequency 2302.5 MHz.

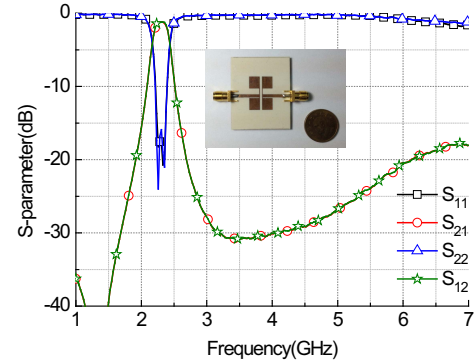


Fig. 9. Measured S-parameters and the photograph of the SIRs based bandpass filter.

### D. Array antennas

The array antenna used in the beamformer and AOA estimator is comprised of 8 subarrays, each containing a uniform linear array with 10 microstrip antennas, as shown in Fig. 10. The antenna array is implemented on a microwave dielectric substrate (RO4003) whose thickness is 0.8mm; the photo of the array antenna is shown in Fig. 10. The distance between the two adjacent subarrays is 15.6 mm. The simulated and measured reflection coefficient ( $S_{11}$  in dB) of each subarray antenna is shown in Fig. 11. The measured impedance bandwidth for  $S_{11} = -15$  dB is from 9350 MHz to 9520 MHz. A simulation of the radiation angle of the main beam of the single subarray showed less than 1.5 degrees of angular variation due to frequency scan from 9350 MHz to 9550 MHz. Figure 12 and 13 show the simulated and measured radiation patterns of each subarray antenna at 9410 MHz in the  $x-z$  plane (H-plane) and  $y-z$  (E-plane) plane, respectively. Fig. 12 shows that the measured antenna gain, the half-power beam-width, and the side-lobe level are 16 dBi,  $9^\circ$ , and -15 dB, respectively. The half-power beam-width and the side-lobe level on the  $y-z$  plane were  $98^\circ$  and -13.5 dB, respectively. Due to the angle-of-arrival application, a wide field-of-view is needed for each subarray in the  $y-z$  plane. It is apparent that generally the agreement between the measurement and simulation results is

good.

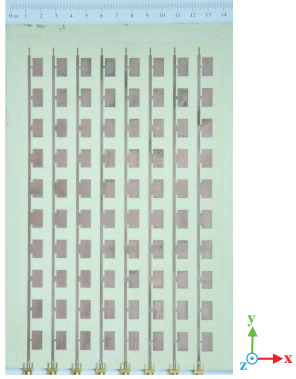


Fig. 10. Photograph of the array antennas consisting of 8 subarray antennas made of 1D patches array; the  $x$ -axis is along the 1D micro-strip array and the  $y$ -axis is along the direction of SMA connectors array.

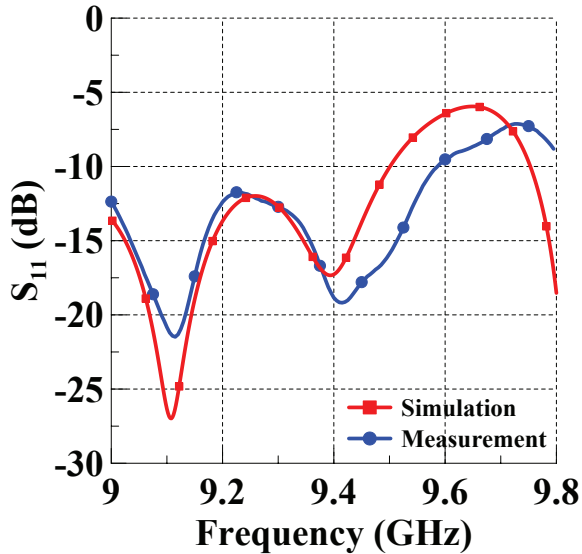


Fig. 11. Measured  $S_{11}$  of the subarray antenna (1D patches array).

#### IV. HYBRID ANALOG-DIGITAL BEAMFORMER

##### A. System architecture of the beam-forming network

Figure 14 shows the system block of the beam-former consisting of an array with 8 transmitters, each of which converts a linear FM from IF (from 175 MHz to 225 MHz) to X-band, centered at 9410 MHz. Only a single receiver is presented in the figure. The aforementioned phased local oscillator was implemented in the design to serve as an analog beam-former. The linear FM signal generated by the direct digital synthesizer (two pieces of AD9959) can provide 8 independent channel signals, if necessary, with programmable phase angle and amplitude, and the digital beam-forming can be achieved by using this system. Each of the transmitters has an architecture similar to the single channel FMCW described

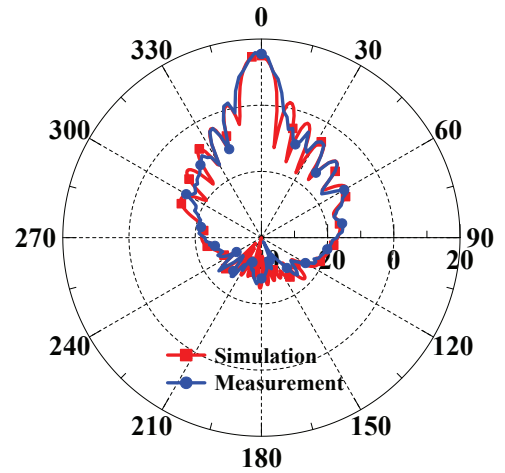


Fig. 12. Simulated and Measured radiation pattern on the  $x$ - $z$  plane (H-plane) of the antenna shown in Fig. 10.

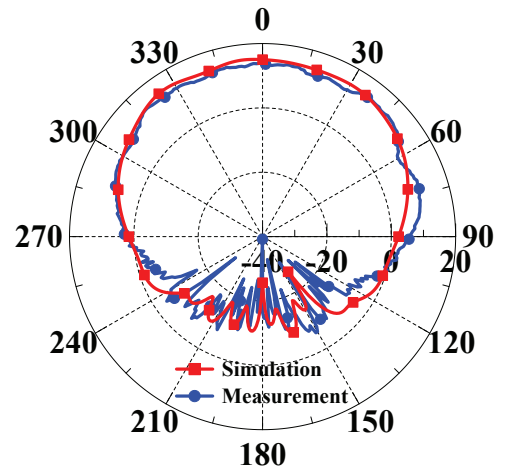


Fig. 13. Simulated and Measured radiation pattern on the  $y$ - $z$  plane (E-plane) of the antenna shown in Fig. 10.

previously. To maintain the same phase angle among the eight phased local oscillators, the sinusoidal signal of 2302.5 MHz VCO is fed into a 1-to-8 power divider based on the Wilkinson architecture. The phased local oscillator while operating together with the phase shifter, frequency multipliers, band-pass filters and low-noise amplifiers, has the output power of +7 dBm and phase noise of -110 dBc/Hz at 1 MHz offset from 9210 MHz carrier frequency. Specifically, for the purpose of phase calibration, some of the X-band signal in each channel is coupled (through a T-junction SMA connector) and converted into I/Q baseband through an IQ demodulator to measure their phase angle and amplitude. In this manner, we can calibrate the phase angle of each channel by adjusting the angle of each of the voltage-controlled phase shifter.

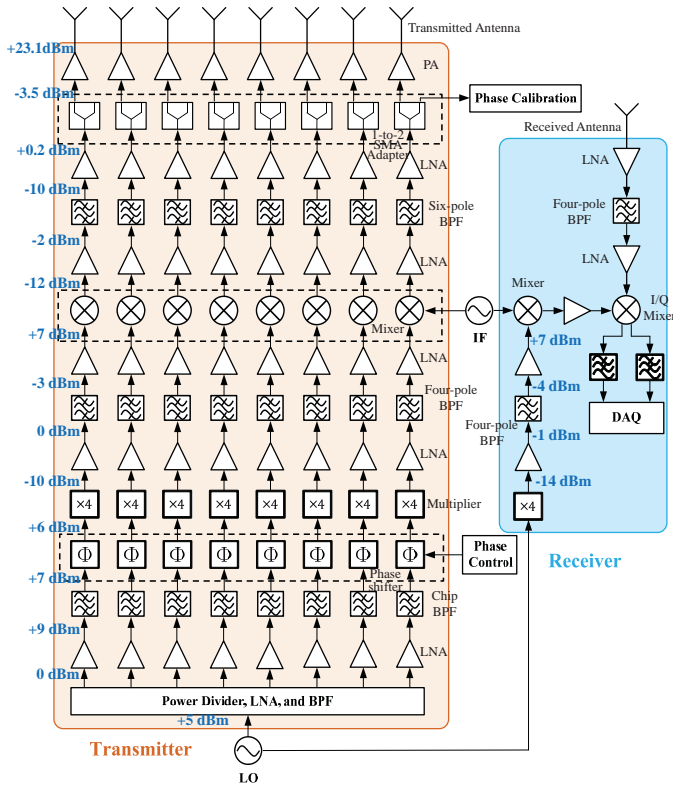


Fig. 14. System block diagram of the beamformer consisting of 8 FMCW transmitters array.

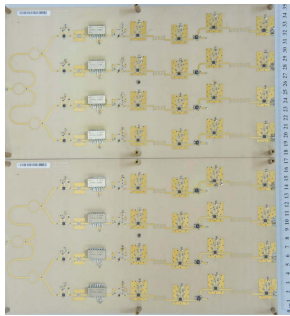


Fig. 15. Photo of the beamformer module.

**B. Radiation pattern measurement of the beamformer plus subarray antennas**

Figures 16 and 17 show the simulated and measured radiation patterns for the phased-array antenna after the analog beam-forming. Altering the progressive phase delay angle among the phased local oscillators swings the main beam pattern. The progressive phase delay angle corresponding to each pattern is indicated in the legend. Each of the measured pattern can generally agree with the simulated one except for the sidelobe level. It is conjectured that the imperfect tapering over the amplitude distribution of the subarrays results in high sidelobe levels. However, the situation can be improved by using digital beam-forming technology and letting the DDS

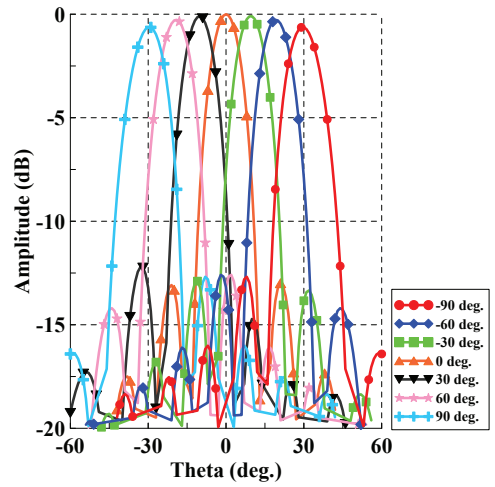


Fig. 16. Simulated radiation pattern with beam-forming.

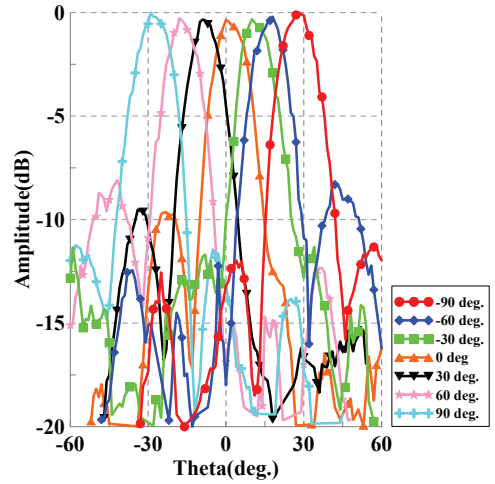


Fig. 17. Measured radiation pattern with beam-forming .

manipulate the amplitude and phase of the IF FMCW signal. Additionally, the measured (simulated) main beam angles are 28°(30°), 18°(20°), 10°(10°), 0°(0°), -9°(-10°), -18°(-20°), and -29°(-30°), respectively. The measured 3 dB beam-width is around 13°, on average.

**V. ANGLE-OF-ARRIVAL ESTIMATOR**

**A. Multiple Signal Classification: MUSIC**

An angle-of-arrival estimation algorithm was developed to estimate the direction of the incoming signals through processing the data received by each of the array antennas. In comparison with the classical methods, which first compute a spatial spectrum and then estimate the angles of arrival by searching the local maxima of the spectrum, the multiple signal classification (MUSIC) algorithm can achieve a higher angular resolution via the subspace method. The mathematical formulation of the MUSIC algorithm is introduced as follows.

Assume an 1-D antenna array with  $N$  elements that are arranged along the  $y$ -axis with a spacing  $d$ . Let us assume that there are  $M$  ( $M < N$ ) incident electromagnetic waves arriving from different angles. First of all, let us consider the case where the incident waves may have different angles along the elevation direction ( $\theta$ ), but have the same azimuthal angle ( $\phi$ ), which is set to zero. Therefore, the received signal at each of the antennas, contributed by the  $M$  incident waves, is expressed as:

$$x_n(k) = \xi_n(k) + \sum_{i=1}^M s_i(k) e^{ik_o n d \sin \theta_i} \quad (9)$$

with the index  $k$  representing the  $k^{th}$  snapshot (or sample).

The parameter  $\xi_n(k)$  is the noise amplitude received by the  $n^{th}$  antenna. The parameter  $s_i(k)$  is the amplitude of the  $i^{th}$  incident wave, which is a complex number in general. We collect the received signals at each of the antenna and arrange them in a column vector, which is written as follows:

$$\underline{x}(k) = A\underline{s}(k) + \underline{\xi}(k) \quad (10)$$

The matrix  $A$  has the size  $N \times M$  with its  $j^{th}$  column  $\underline{a}(\theta_j)$  representing the steering vector of the  $j^{th}$  signal with the incident angle  $\theta_j$ , written below:

$$\underline{a}(\theta_j) = (1 \ e^{ik_o d \sin \theta_j} \ e^{i2k_o d \sin \theta_j} \ \dots \ e^{i(N-1)k_o d \sin \theta_j})^T \quad (11)$$

, where  $j$  ranges from 1 to  $M$ .

The column vector  $\underline{s}$  has the dimension  $M \times 1$ , and represents the incoming signals. The quantity  $\underline{\xi}$  in (10) is a measure of the white Gaussian noise received by each antenna with the size  $N \times 1$ .

Here, the noise in each channel is supposed to be highly uncorrelated, enabling us to diagonalize the correlation matrix. Consequently, the correlation matrix of  $\underline{x}(k)$  can be written as:

$$R_{xx} = E[\underline{x} \underline{x}^H] = A R_{ss} A^H + R_{nn} \quad (12)$$

, where  $H$  is the Hermitian operator (conjugate transpose), and  $E$  is the statistical average (expected value). The quantities  $R_{ss}$  and  $R_{nn}$  are the source and noise correlation matrices, respectively, and are defined as follows:

$$R_{ss} = E[\underline{s} \underline{s}^H] \quad (13)$$

$$R_{nn} = E[\underline{\xi} \underline{\xi}^H] = \sigma^2 \mathbf{I} \quad (14)$$

The matrix  $R_{xx}$  has  $M$  eigenvectors associated with the  $v_j$  signals with  $j=1,2,3,\dots,M$ , and it has  $N-M$  eigenvectors related to the noise. We can construct a new subspace by using the  $N-M$  noise eigenvectors, and write it as follows:

$$V_{noise} = [v_{M+1} \ v_{M+2} \ \dots \ v_N] \quad (15)$$

It is possible to prove that the noise subspace eigenvector in (15) is orthogonal to the steering matrix in (11). Moreover, the

pseudo-spectrum  $P_{pseudo}(\theta)$  defined by the MUSIC algorithm can be written as:

$$P_{pseudo}(\theta) = \frac{1}{\sum_{m=M+1}^N |A^H(\theta)v_m|^2} \quad (16)$$

Owing to the orthogonality between the signal steering and noise vectors, the denominator in (16) becomes zero when  $\theta$  corresponds to a signal direction. Therefore, there would be  $M$  peaks in the pseudo-spectrum distribution, which correspond to the directions of arrival of the signal.

### B. Spatial Smooth MUSIC

The traditionally used MUSIC assumes that all arrival signals are uncorrelated (the signal correlation matrix in (13) is a diagonal matrix). In the radar detection scenario, the scattering waves are indeed correlated because they originate from the transmitting antenna. The correlation reduces the rank of the signal correlation matrix in (13), causing the number of noise eigenvectors to be greater than  $N-M$ .

To overcome this problem, the spatial smoothing MUSIC algorithm is employed. First, the original array is subdivided into 5 overlapped subarrays, each with 4 elements. For example, the first subarray contains the antennas (1, 2, 3, 4); the second one includes (2, 3, 4, 5); the third one is (3, 4, 5, 6); the fourth one is (4, 5, 6, 7); and the last one is (5, 6, 7, 8). The correlation matrix corresponding to each subarray can be obtained and denoted by  $R_j$ , whose dimensions are  $4 \times 4$ , where  $j$  varies from 1 to 5. The MUSIC algorithm is then applied for the *smoothed* correlated matrix, given below:

$$R_{smooth} = \frac{1}{5} \sum_{j=1}^5 R_j \quad (17)$$

The matrix  $R_{smooth}$  above becomes full-rank once again. Consequently, the above formulation can detect the arrival angles up to 4 correlated signals.

### C. AOA Estimator Architecture

The system architecture for implementing the MUSIC/smooth MUSIC is shown in Fig. 18. The photo of the fabricated AOA estimator is shown in Fig. 19. Recall that the receiving antenna was shown earlier in Fig. 10. For each of the subarrays, the main beamwidth is narrower along the vertical direction, whereas the beamwidth along the horizontal direction is wider. The receiving antenna is connected to a low-noise amplifier and a band-pass filter. Furthermore, the received signal is converted into the baseband I and Q by beating it with that of the local oscillator (the received signal is a complex number). The baseband signals of each channel can be further sampled by using a data acquisition system. The arrival angles of the correlated signals can be estimated by using the spatial smoothing MUSIC algorithm described previously. It is worth mentioning that the calibration must be carried out initially to equalize the phases and amplitudes among the eight channels. We may feed each channel by an in-phase signal to calibrate their amplitudes and phases at their

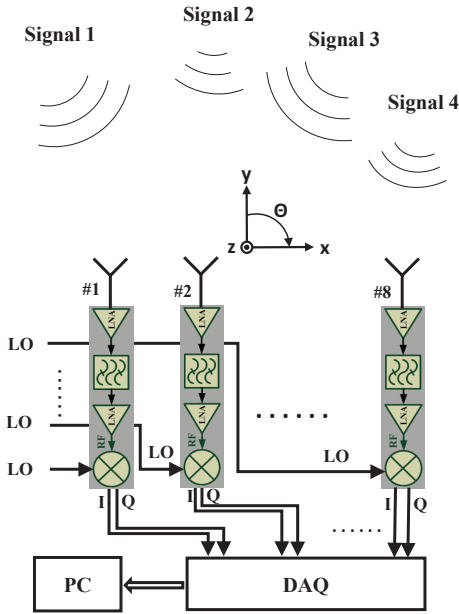


Fig. 18. System block diagram of an AOA estimator.

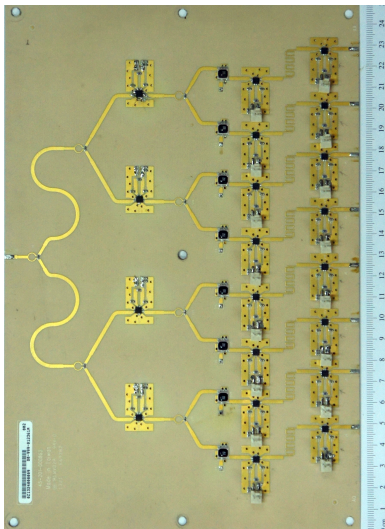


Fig. 19. Photo of the module of AOA estimator.

baseband frequencies after their down-conversion. Specifically, the weighting factor of each channel is prescribed at baseband.

Figures 20 and 21 show the distribution of the pseudo spectrum against the incident angle  $\theta$ , derived by using the MUSIC and spatially smoothed MUSIC algorithms, respectively. The three correlated signals have the same amplitude but different prescribed incident angles, namely  $52^\circ$ ,  $33^\circ$ , and  $-10^\circ$ . Apparently, in Fig. 20, the commonly used MUSIC algorithm cannot handle the correlated signals; however, the spatially smoothed MUSIC can correctly estimate the three incident angles. The figures were obtained via computer simulation of the following example. We will demonstrate the use of the

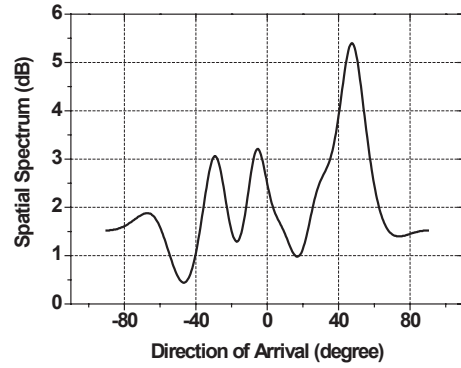


Fig. 20. Pseudo spectrum computed by traditionally used MUSIC

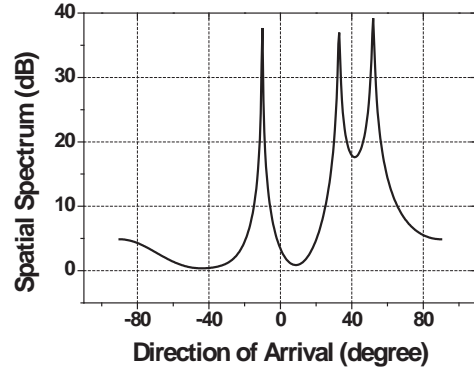


Fig. 21. Pseudo spectrum computed by smoothed MUSIC

measured results obtained by processing the data through our hardware and software systems.

Figure 22 shows the measured results and the testing environment for the AOA estimation. Two trihedrals were placed in front of the receiving arrays, consisting of an 8 1-D patch array – the receiver architecture is shown in Fig. 18. A transmitting antenna, whose field-of-view is able to cover the two trihedrals, is taken as the illuminator, enabling the echo signals received by the array antennas. We employ the trihedral because its RCS is less sensitive to the variation of the incident angle within certain range of the angular spectrum. It is obvious from the result shown in this figure that the two targets can be correctly identified through our AOA estimator in a complex outdoor environment.

## VI. RADAR PERFORMANCE EVALUATION

In the previous sections, we have discussed the theoretical and experimental studies of the FMCW radar transmitter, receiver, beamformer, AOA estimator and phased array antennas. In this section, we focus on the performance evaluation of the FMCW radar system incorporating the phased array system. Specifically, we demonstrate the detection of the range and azimuth angle of the echo signals reflecting from targets to evaluate the performance of the radar system. Additionally, the assessment of range resolution is also carried out by using the radar target simulator.

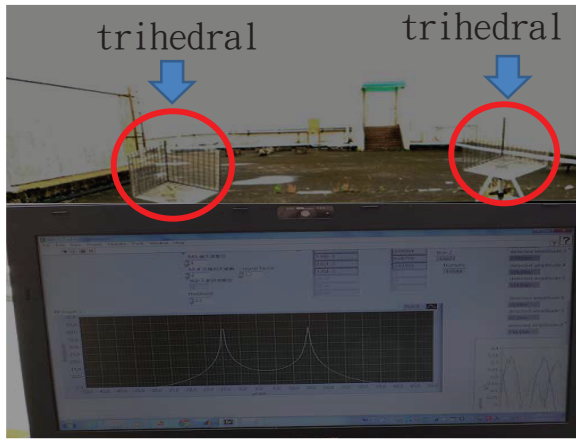


Fig. 22. AOA estimation for two scatterers (trihedrals) in an open site.

**A. Radar system analysis**

Before performing the experimental studies, we carry out a system analysis using (5), with parameters given as follows:  $G_t = 15 \text{ dBi}$  (subarray),  $G_r = 22 \text{ dBi}$ ,  $P_t = 0 \text{ dBm}$  (subarray),  $L_s = 8 \text{ dB}$ , and  $NF = 8 \text{ dB}$ . Figure 23 shows the variation of the SNR against the range (in the unit of Km) for various values of RCS ranging from  $100 \text{ m}^2$  to  $500 \text{ m}^2$  with the increment of  $100 \text{ m}^2$ . Considering the rough terrain, the one-way path loss exponent is assumed to be 2.1 for numerical simulations. The detection SNR threshold is set to 12 dB and is shown as the dark yellow line. The maximum detectable range increases in accordance with the increase in the RCS. Isolation between the transmit and receive antennas has been measured more than 70 dB to ensure radar sensitivity.

Additionally, Figure 24 shows the variation of SNR against the range (in the unit of Km) for various values of one-way path loss exponent (PLE) ranging from 2.0 to 2.4 with an increment of 0.1. The RCS is set to be  $500 \text{ m}^2$ . As is well known, the PLE is influenced by terrain contours, environment, propagation medium, polarization of electromagnetic wave and the operating frequency. Apparently, the path loss exponent affects the SNR performance significantly. The larger the PLE is, the smaller the maximum detectable range is. From this figure, we note that the detectable range shrinks to less than 2 kilometers as the PLE becomes 2.4. Conversely, for a long range detection (two-ray ground-reflection model) with the PLE around 2.0, it has the maximum detectable range up to 8 kilometers.

**B. Range detection**

Figure 26 shows the FFT-normalized power in dB – with the receiver phase noise power spectrum removed – versus the range in meters. The peak at around 220 meters, whose SNR is over 15 dB, indicates a target, which is a welded wire mesh fence with a grid-size less than a half-wavelength at 9410 MHz. Moreover, the cluster of peaks around 826 meters, whose associated SNR level is adequate, correspond to a building with its depth exhibited, together with the targets and terrain contour that are shown in Fig. 25.

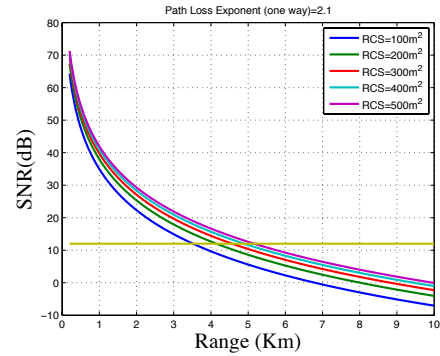


Fig. 23. Variation of SNR versus range for various values of RCS.

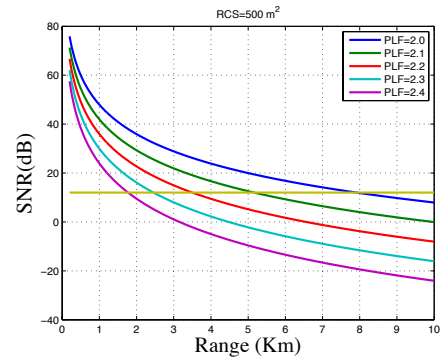


Fig. 24. Variation of SNR versus range for various values of propagation loss exponent.



Fig. 25. Aerial perspective of the targets and terrain contour for radar detection; the phased array radar system is located at the ninth floor, Kuang-Fu campus of National Chiao-Tung University, Hsinchu, Taiwan. Notably, target A is a welded wire mesh fence with the mesh size smaller than half wavelength (9410 MHz) .

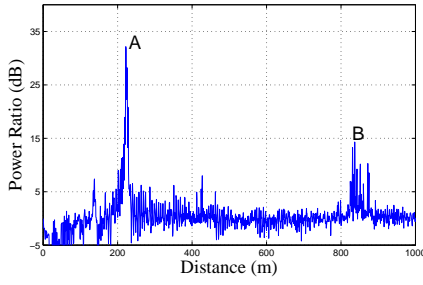


Fig. 26. FFT power ratio (normalized to the background signal) *versus* range of detection.

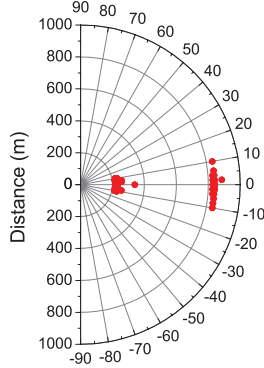


Fig. 27. Echo signals from reflecting objects displayed in plane view with the azimuth angle and range shown in polar coordinate system (plane-position indicator) .

### C. Range and azimuth angle detection

For the detection of range and azimuth angle, beamformer is controlled by a PC which tunes the voltage via a 14-bit DAC; the phase angle on each phased local oscillator is programmable. Consequently, the phased array system can dynamically steer its main beam pattern. In the following example, the phased array radar scans over a field-of-view ranging from  $-10^\circ$  to  $+10^\circ$ . Figure 27 shows the echo signals from reflecting objects displayed in plane view with the azimuth angle and range depicted in a polar coordinate system (plane-position indicator or PPI). The information on the range and azimuth angle of each red dot, corresponding to each scatterer, can be readily extracted from this figure.

Parameter	Value
Maximum Detection Range	37.5 km
Receiver Sensitivity	$-126$ dBm
Field of View	$\pm 30^\circ$
Array Scan Angle	$\pm 30^\circ$
Range Resolution	3 m
AOA Resolution	$0.6^\circ$

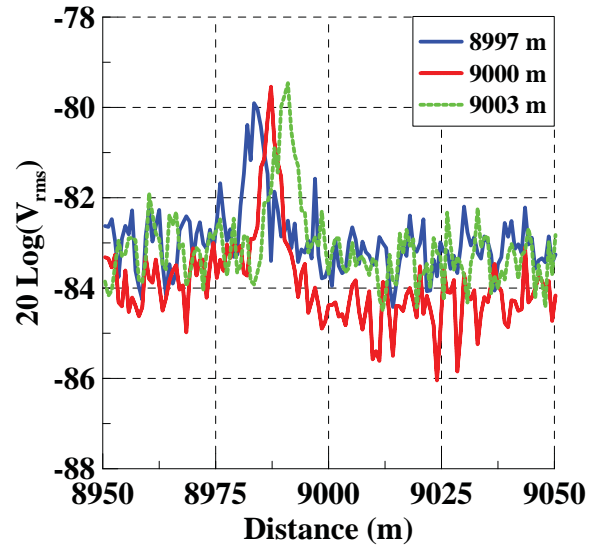


Fig. 28. Range detection measurement via radar target simulator.

### D. Range resolution measurement using a radar target simulator

Range resolution is one of the important factors we consider when evaluating the performance of an FMCW radar. The range resolution is related to the bandwidth of the sweep frequency, as indicated in (4). Based on the above formula, the range resolution is 3 meters for 50 MHz linear FM signal bandwidth. Here, a target simulator is employed for the measurement. The X-band FMCW signal generated by our radar transmitter is fed into a target simulator; the target simulator then manipulates the delay time (to simulate the round trip time) and return to our radar receiver according the prescribed radar cross section and range. The radar cross section is set to be  $500 m^2$ . The three target ranges at 8997 m, 9000 m, and 9003 m are set, respectively. Figure 28 shows the FFT waveform *versus* the range, obtained by using our radar receiver. With the waveform shown in the figure, we believe that we can resolve two targets that are 3 m apart by using this receiver.

## VII. CONCLUSION

In this paper, we have described a 1-D phased-array FMCW marine radar system, operating at the X band. Eight subarray antennas, each consisting of uniform linear arrays that generate a narrow beamwidth along the vertical direction and a wide beamwidth along the horizontal direction, were developed for the beamformer and the AOA estimator. The sweep frequency and time of the FMCW signal are 50 MHz and 0.25 ms, respectively. The range resolution is 3 m, which is verified through the measurements carried out by using a target simulator. Specifically, a phased-stable local oscillator was exploited in the analog beam-forming, whereas the digital beam-forming architecture which manipulates the amplitude and phase over the baseband using direct digital synthesizers was reserved. Regarding the AOA estimator, the smooth-MUSIC algorithm

was employed for the purpose of detecting the correlated echo signal illuminated by a transmitter. The two aforementioned functions were separately verified and excellent performance was demonstrated. Our future work will be directed toward the integration of the two individual systems.

## REFERENCES

- [1] Merrill I. Skolnik, *Introduction to Radar Systems*. McGraw-Hill, 2001.
- [2] Fred E. Nathason, J. Patrick Reilly, Marvin N. Cohen, *Radar Design Principles*. McGraw-Hill, 1991.
- [3] Eli Brookner, *Radar Technology*. Artech House, 1977.
- [4] Martin Jahn, Reinhard Feger, Christoph Wagner, Ziqiang Tong, and Andreas Stelzer, "A Four-Channel 94-GHz SiGe-Based Digital Beamforming FMCW Radar," *IEEE Transactions on Microwave Theory and Techniques*, vol. 60, no. 3, pp. 861 – 869, Mar. 2012.
- [5] F.-Y. Kuo and R.B. Hwang, "High-Isolation X-Band Marine Radar Antenna Design," *IEEE Transactions on Antennas and Propagation*, vol. 62, pp. 2331–2337, May 2014.
- [6] Barry D. Van Veen and Kevin M. Buckley, "Beamforming: A versatile Approach to Spatial Filtering," *IEEE ASSP Magazine*, vol. 5, no. 2, pp. 4 – 24, Apr. 1988.
- [7] V. U. Reddy, A. Paulraj, and T. Kailath, "Performance analysis of the optimum beamformer in the presence of correlated sources and its behavior under spatial smoothing," *IEEE Trans. Acoust., Speech, Signal Processing*, vol. 35, no. 7, pp. 927 – 936, July 1987.
- [8] D. Kelley and W. Stutzman, "Array antenna pattern modeling methods that include mutual coupling effects," *IEEE Transactions on Antennas and Propagation*, vol. 41, no. 12, pp. 1625 – 1632, Dec. 1993.
- [9] H. Aumann, A. Fenn, and F. Willwerth, "Phased array antenna calibration and pattern prediction using mutual coupling measurements," *IEEE Transactions on Antennas and Propagation*, vol. 37, no. 7, pp. 844 – 850, July 1989.
- [10] A. Paulraj and T. Kailath, "Eigenstructure method for direction of arrival estimation in the presence of unknown noise field," *IEEE Trans. Acoust., Speech, Signal Processing*, vol. 34, no. 1, pp. 13 – 20, Feb. 1986.
- [11] J. C. Liberti and T. S. Rappaport, *Smart antennas for wireless communications: IS-95 and third generation CDMA applications*. Prentice Hall PTR, 1999.
- [12] L. C. Godara, "Application of Antenna Arrays to Mobile Communications. II. Beamforming and Direction-of-Arrival considerations," *Proceedings of IEEE*, vol. 85, no. 8, pp. 1195 – 1245, Aug. 1997.
- [13] T. K. Sarkar, Michael C. Wicks, M. Salarzar-Palma, Robert J. Bonneau, *Smart Antennas*. John Wiley & Sons, 2005.
- [14] Frank Gross, *Smart antenna for wireless communications*. McGraw-Hill, 2005.
- [15] R. O. Schmidt, "Multiple emitter location and signal parameter estimation," *IEEE Transactions on Antennas and Propagation*, vol. 34, no. 3, pp. 276 – 280, Mar. 2003.
- [16] S. U. Pillai, and B. H. Kwon, "Performance Analysis of MUSIC-type High Resolution Estimators for Direction Finding in Correlated and Coherent Scenes," *IEEE Transactions on Acoustics, Speech and Signal Processing*, vol. 37, no. 8, pp. 276 – 280, Aug. 1989.
- [17] T. J. Shan, M. Wax, and T. Kailath, "On spatial smoothing for direction-of-arrival estimation of coherent signals," *IEEE Transactions on Acoustics, Speech and Signal Processing*, vol. 33, no. 4, pp. 806 – 811, Jan. 1985.
- [18] H. Krim, J. G. Proakis, "Smoothed Eigenspace-Based Parameter Estimation," *Automatica*, vol. 30, no. 1, pp. 17 – 38, 1994.
- [19] J.-S. Hong and M. J. Lancaster, *Microstrip filters for RF/microwave applications*. John Wiley & Sons, 2004, vol. 167.
- [20] J.-S. Hong and M. J. Lancaster, "Couplings of microstrip square open-loop resonators for cross-coupled planar microwave filters," *IEEE Transactions on Microwave Theory and Techniques*, vol. 44, no. 11, pp. 2099–2109, 1996.
- [21] J.-T. Kuo, W.-H. Hsu, and W.-T. Huang, "Parallel coupled microstrip filters with suppression of harmonic response," *IEEE Microwave and Wireless Components Letters*, vol. 12, no. 10, pp. 383–385, 2002.
- [22] J.-T. Kuo, S.-P. Chen, and M. Jiang, "Parallel-coupled microstrip filters with over-coupled end stages for suppression of spurious responses," *IEEE Microwave and Wireless Components Letters*, vol. 13, no. 10, pp. 440–442, 2003.
- [23] J. T. Kuo and E. Shih, "Microstrip stepped impedance resonator bandpass filter with an extended optimal rejection bandwidth," *IEEE Transactions on Microwave Theory and Techniques*, vol. 51, no. 5, pp. 1554–1559, 2003.
- [24] D. M. Pozar, *Microwave engineering*, 3rd ed. New York: Wiley, 2004.
- [25] "CST studio suite 2012," <http://www.cst.com>.

**Ruey-Bing (Raybeam) Hwang** earned his B.S. at Department of Communications Engineering, National Chiao-Tung University in 1990, and M.S. at Department of Electrical Engineering, National Taiwan University in 1992. He received the Ph. D. degree in Institute of Electronic Engineering, National Chiao-Tung University in 1996. From August 2004 to July 2005, he was an Assistant Professor at the Communication Engineering Department, National Chiao-Tung University. He became a professor of ECE Department in August 2008. He is the director of Phased-Array Technology Laboratory, ECE Department, National Chiao Tung University. In August 2013, he was appointed Director of the Graduate Institute of Communications Engineering, which is affiliated with the ECE Department. Currently Prof. Hwang is the Chair of IEEE AP-S Taipei Chapter. Prof. Hwang has authored or co-authored over 100 journal and international conference publications in the area of microwaves, optics and applied physics. Additionally, he authored a book entitled *Periodic Structures: Mode-Matching Approach and Applications in Electromagnetic Engineering*, published by Wiley-IEEE Press, 2013. His research interests include electromagnetic periodic structure theory, optical grating theory, phased array theory, antennas design, FMCW radar system, and electromagnetic compatibility. He is an honour member of Phi Tau Phi.

**Yi-Che Tsai** is currently working towards the Ph. D. degree in Graduate Institute of Communications Engineering, National Chiao Tung University, Hsinchu, Taiwan.

**Chun-Fan Chien** is currently working towards the Master degree in Graduate Institute of Communications Engineering, National Chiao Tung University, Hsinchu, Taiwan.

**Fang-Yao Kuo** is currently working towards the Ph. D. degree in Graduate Institute of Communications Engineering, National Chiao Tung University, Hsinchu, Taiwan.

**Hsien-Tung Huang** is currently working towards the Ph. D. degree in Graduate Institute of Communications Engineering, National Chiao Tung University, Hsinchu, Taiwan.

**Wei-Hsiung Chen** is a Assistant VP, PBU 1, ZyFlex Technology, Hsinchu 30075, Taiwan. He earned his Ph. D. degree from Department of Electrical Engineering, University of Southern California.

**Cherng-Chyi Hsiao** is a researcher in Phased-Array Technology Laboratory, ECE Department, National Chiao Tung University, Hsinchu, Taiwan. He received his Ph. D. degree from Graduate Institute of Communications Engineering, National Chiao Tung University, Hsinchu, Taiwan, in 2004.

**Chin-Cheng Chuang** is currently working towards the Master degree in Graduate Institute of Communications Engineering, National Chiao Tung University, Hsinchu, Taiwan.

**Ke-Wen Lin** is currently working towards the Master degree in Graduate Institute of Communications Engineering, National Chiao Tung University, Hsinchu, Taiwan.

**Yuan-Hao Sun** is currently working towards the Master degree in Graduate Institute of Communications Engineering, National Chiao Tung University, Hsinchu, Taiwan.